Significant electron-magnon scattering in layered ferromagnet Cr_2Te_3

Yujun Wang,[1] Shunzhen Wang,[1] Masashi Kawaguchi,[1] Jun Uzuhashi,[2] Akhilesh Kumar Patel,[2] Kenji Nawa,[3,2,*] Yuya Sakuraba,[2] Tadakatsu Ohkubo,[2] Hiroshi Kohno,[4] and Masamitsu Hayashi[1,5,†]

[1] *Department of Physics, The University of Tokyo, Tokyo 113-0033, Japan*

[2] *National Institute for Materials Science, Tsukuba 305-0047, Japan*

[3] *Graduate School of Engineering, Mie University, Tsu 514-8507, Japan*

[4] *Department of Physics, Nagoya University, Nagoya 464-8602, Japan*

[5] *Trans-scale quantum science institute, The University of Tokyo, Tokyo 113-0033, Japan*

Abstract

A layered ferromagnet Cr_2Te_3 is attracting growing interest because of its unique electronic and magnetic properties. Studies have shown that it exhibits sizable anomalous Hall effect (AHE) that changes sign with temperature. The origin of the AHE and the sign change, however, remains elusive. Here we show experimentally that electron-magnon scattering significantly contributes to the AHE in Cr_2Te_3 through magnon induced skew scattering, and that the sign change is caused by the competition with the Berry-curvature or impurity-induced side-jump contribution. The electron-magnon skew scattering is expected to arise from the exchange interaction between the itinerant Te *p*-electrons and the localized Cr *d*-electrons modified by the strong spin-orbit coupling on Te. These results suggest that the magnon-induced skew scattering can dominate the AHE in layered ferromagnets with heavy elements.

* current affiliation: National Institute of Advanced Industrial Science and Technology, Tsukuba 305-8568, Japan

† hayashi@phys.s.u-tokyo.ac.jp

I. INTRODUCTION

The Cr-Te compound[1] is a material system that has attracted significant interest recently owing to its unique structural, transport and magnetic properties. Many of the compounds form a layered structure and are stable down to a monolayer. The majority of the compounds exhibit strong ferromagnetism with some exceptions (e.g. antiferromagnetism in $CrTe_3$[2] and $Cr_{1+\delta}Te_2$[3]). Studies have shown that ferromagnetism persists down to a monolayer[4], allowing studies on two-dimensional magnetism[5–7]. The Curie temperature typically lies in a range of 100 K to 200 K. With proper growth conditions[8, 9], however, recent reports show the Curie temperature can be increased, exceeding room temperature under certain circumstances[4, 10, 11]. Owing to the crystalline anisotropy, the magnetic easy axis often points along the film normal, with the perpendicular magnetic anisotropy energy larger than that of other layered ferromagnets[12, 13].

The transport properties of the compounds also show unique characteristics. In particular, the compound exhibits a sizable anomalous Hall effect[14–16]. Studies have shown that the anomalous Hall resistance changes its sign as the temperature is varied[9, 15, 17–21]. The origin of the anomalous Hall effect as well as its sign change with temperature have been under scrutiny. It has been reported that the anomalous Hall effect in the Cr-Te compounds is caused by the large Berry curvature of the bands near the Fermi level[18, 20–23]. As the Berry curvature induced anomalous Hall conductivity was found to be an odd function of energy, it causes a sign change in the anomalous Hall resistance as the temperature is varied due to population change of the occupied bands. However, other studies[14, 15, 24] have shown that contribution from the skew scattering plays an essential role in the anomalous Hall effect, posing question on its origin.

Here we show that the unique characteristics of the anomalous Hall effect in Cr_2Te_3, one of the most stable compounds in the Cr-Te family, are defined by electron-magnon scattering. Cr_2Te_3 has a layered structure in which layers of $CrTe_2$ are connected by intercalated Cr atoms. We find the electron-magnon scattering significantly contributes to the longitudinal and anomalous Hall resistances. The scaling relation between the longitudinal and anomalous Hall resistivities is used to identify the origin of the anomalous Hall effect. We find two competing sources: magnon induced skew scattering and impurity induced side jump/Berry curvature effect. Model calculations show that the former is caused by the exchange interaction between the itinerant Te p-electrons and the localized Cr d-electrons modified by the spin-orbit coupling. We consider Te, which possess significant spin-orbit coupling, plays a critical role in setting the magnon-induced skew scattering.

II. EXPERIMENTAL RESULTS

A. Structural and magnetic properties

Cr_2Te_3 films were grown on sapphire or MgO substrates using molecular beam epitaxy (MBE). A Ti or Te layer was used as a capping layer. See "Methods" and Supplementary Note 1 for the details of sample preparation and characterization. A cross-sectional high-angle annular dark-field scanning transmission electron microscopy (HAADF-STEM) image of a 20 nm-thick Cr_2Te_3 film is displayed in Fig. 1(a). The bright and dark contrasts of the image represent grains with different crystal orientations within the film plane. The grain size is of the order of a few tens of nanometers. The high magnification image, Fig. 1(c), and the corresponding nanobeam electron diffraction pattern, Fig. 1(d), show highly textured film with growth along the Cr_2Te_3 (001) direction. Energy dispersive X-ray spectroscopy (EDS) maps of the elements are shown in Fig. 1(b). The images show Cr and Te are uniformly distributed within the film. Profile of the film composition along the film normal is presented in Fig. 1(e). From the profile, we determine the film composition is Cr:Te $\sim$ 2:3. See Supplementary Figure S1 for the reflection high energy electron diffraction (RHEED) images and the X-ray diffraction (XRD) spectra of the films.

First, we study the magnetic properties of Cr_2Te_3. Figure 2(a) shows the temperature dependence of the saturation magnetization M_s for films with different thicknesses. The Curie temperature T_C is $\sim$175 K for all samples except for the 5 nm-thick film, which exhibits T_C of $\sim$215 K. See Supplementary Note 2 for the details of how T_C is extracted. The value of M_s at 2 K for the thicker films is close to that predicted from first principles calculations, which is $\sim$465 emu/cm^3. We find M_s is substantially larger for the thinner films (5 nm and 10 nm-thick). Previous studies have reported that the magnetic moments of Cr_2Te_3 are canted from the film normal but the canting can be suppressed when the film thickness is reduced, thereby causing a difference in M_s against the film thickness[13]. Alternatively, it has been shown, using scanning tunnel microscopy, that Cr_3Te_4 forms at the beginning of the growth with molecular beam epitaxy[25]. Since the saturation magnetization of Cr_3Te_4 is larger than that of Cr_2Te_3[26, 27], the magnetization can be larger for the thinner films given the larger weight of the Cr_3Te_4 phase. Note that the transport properties of Cr_3Te_4[28, 29] are not significantly different from those of Cr_2Te_3. In addition, M_s shows an upturn below ~10 K for the thinner films. Such change in M_s at low temperature was reported previously[9]. Although the physical mechanism behind the upturn is unclear in Cr_2Te_3, previous studies for other systems (e.g. ultra-fine cobalt ferrite nanoparticles) suggested that it may originate from surface magnetic moments[30]. Further study is required to clarify the origin of the thickness dependence of M_s and the upturn below ~10 K. In Supplementary Figure S2, we show a few exemplary magnetization hysteresis loops. The loops show that the magnetic easy axis of the films points along the film normal, in agreement with previous studies[24]. For later use, we define M_s^0 as M_s obtained at the lowest measurement temperature (~2 K).

B. Longitudinal transport properties

The transport properties are studied using the patterned Hall bars: see Supplementary Note 2 and Figure S3 for the details of the device structure. The temperature dependence of the longitudinal resistivity ρ_{xx} of a 10 nm-thick film is shown in Fig. 2(b). We find the temperature dependence of ρ_{xx} for $T < T_\mathrm{C}$ can be fitted with the following function:

$$\rho_{xx} = \rho_{xx}^0 + \rho_{xx}^\mathrm{m} T^2 \quad (T < T_\mathrm{C}). \tag{1}$$

The fitting result, shown by the red solid line in Fig. 2(b), is in good agreement with the experimental results. The change in ρ_{xx} for $T > T_\mathrm{C}$ is almost linear and its slope is small: see also Supplementary Figure S4.

The quadratic temperature dependence of ρ_{xx} below T_C can be attributed to electron-magnon scattering[31, 32]. (As is often the case in metals[32], we neglect electron-electron scattering, which also scales with T^2.) The temperature independent resistivity that is dominant at the lowest temperature is likely associated with impurity induced scattering. We therefore assign ρ_{xx}^0 and ρ_{xx}^m as the impurity and electron-magnon scattering coefficients, respectively. The film thickness dependences of ρ_{xx}^0 and ρ_{xx}^m are shown in Figs. 2(c) and 2(d), respectively. ρ_{xx}^0 tends to decrease with film thickness, suggesting that the film quality improves for thicker films. In contrast, ρ_{xx}^m increases with the film thickness until it saturates at ~50 nm.

To show that electron-magnon scattering indeed contributes to the transport properties, the out of plane magnetic field (H_z) dependence of the longitudinal resistivity $\Delta\rho_{xx} \equiv \rho_{xx}(H) - \rho_{xx}(H = 0)$ is studied. Figure 3(a) shows representative results from a 10 nm-thick film. There are at least two major effects known to contribute to $\Delta\rho_{xx}$ in magnetic materials[33]: the Lorentz magnetoresistance and the magnon-induced magnetoresistance. Whereas the resistance quadratically increases with H_z for the former, it linearly decreases with H_z for the latter. As is evident, $\Delta\rho_{xx}$ decreases almost linearly with increasing H_z when the temperature is lower than T_c, suggesting that the magnon-induced magnetoresistance is dominant[33]. We fit the data with a linear function near zero field (from ~0 to 10 kOe) to obtain the slope of $\Delta\rho_{xx}$ vs. H_z, which is defined as $\frac{\partial\Delta\rho_{xx}}{\partial H_z}$. $\frac{\partial\Delta\rho_{xx}}{\partial H_z}$ is plotted as a function of temperature for all films in Fig. 3(b). Clearly, $\frac{\partial\Delta\rho_{xx}}{\partial H_z}$ increases as the temperature approaches T_c, suggesting that magnon-scattering plays a larger role at higher temperatures.

In Fig. 3(c-e), we plot $\frac{\partial\Delta\rho_{xx}}{\partial H_z}$ vs. ρ_{xx}^{m} to study if they are correlated. At the lowest temperature [Fig. 3(c)], there is no significant correlation between the two quantities, as magnon-scattering is suppressed in this temperature range. As the temperature is raised[Fig. 3(d,e)], we observe a positive correlation between the two, indicating that $\frac{\partial\Delta\rho_{xx}}{\partial H_z}$ is dependent on magnon-scattering.

C. Anomalous Hall resistance

Next, we study the transverse resistivity ρ_{yx} of Cr_2Te_3. The H_z dependence of ρ_{yx} of a 10 nm-thick film, measured at different temperatures, are plotted in Fig. 4(a). A clear hysteresis loop is observed at temperatures below T_C. The small hump near the magnetization switching fields may be due to the topological Hall effect or the superposition of competing anomalous Hall effects with opposite signs. Although similar features have been observed in other systems and were attributed to the topological Hall effect, e.g. Cr_5Te_6[34], $CrTe_2/Bi_2Te_3$[35] and Cr_2Te_3/Cr_2Se_3[36], we cannot identify its origin in Cr_2Te_3 single layer film from the current data set. The anomalous Hall resistivity $\Delta\rho_{yx}$ is obtained by subtracting the linear background found at high magnetic field and taking half the difference of the background subtracted ρ_{yx} at positive and negative H_z. The linear background is predominantly caused by the ordinary Hall effect: see Supplementary Figure S5 for the carrier density and mobility estimated from the background signal. We normalize $\Delta\rho_{yx}$ with $\frac{M_s}{M_s^0}$ to exclude the temperature dependence of M_s from $\Delta\rho_{yx}$[37]. The normalized anomalous Hall resistivity $\Delta\tilde{\rho}_{yx} \equiv \Delta\rho_{yx}/\frac{M_s}{M_s^0}$ is plotted as a function of temperature in Fig. 4(b). (See Supplementary Figure S4 for the temperature dependence of $\Delta\rho_{yx}$.) As is evident, $\Delta\tilde{\rho}_{yx}$ changes its sign at $T \sim 100$ K, a trend that has been reported in previous studies[9, 15, 17, 20]. Similar to ρ_{xx}, $\Delta\tilde{\rho}_{yx}$ exhibits a T^2 scaling. The red solid line in Fig. 4(b) shows a parabolic fitting, which agrees well with the data. Later, we show that such T^2 scaling is one of the characteristics of magnon-induced skew scattering.

The scaling relation between the anomalous Hall and the longitudinal resistivities is studied to identify the origin of the anomalous Hall effect[38–40]. $\Delta\tilde{\rho}_{yx}$ is plotted against ρ_{xx} in Fig. 4(c). $|\Delta\tilde{\rho}_{yx}|$ increases with increasing ρ_{xx}, with the temperature as an implicit parameter, exhibiting a predominantly linear scaling. In general, the scattering sources that cause the temperature dependence of the anomalous Hall resistivity can be classified into two categories, static and dynamic disorders. The former is caused by impurities and scales with ρ_{xx}^0, whereas the latter can be induced by magnons and phonons and is proportional to $\rho_{xx}^T \equiv \rho_{xx} - \rho_{xx}^0$. From multi-variable scaling derived by Hou *et al.*[39], the anomalous Hall resistivity can be expressed as:

$$\begin{aligned}\Delta\tilde{\rho}_{yx} &= \Delta\tilde{\rho}_{yx}^{\text{skew}} + \Delta\tilde{\rho}_{yx}^{\text{sj}} + \Delta\tilde{\rho}_{yx}^{\text{int}},\\ \Delta\tilde{\rho}_{yx}^{\text{skew}} &= a_1\rho_{xx}^0 + a_2\rho_{xx}^T,\\ \Delta\tilde{\rho}_{yx}^{\text{sj}} &= b_1(\rho_{xx}^0)^2 + b_2(\rho_{xx}^T)^2 + b_3\rho_{xx}^0\rho_{xx}^T,\\ \Delta\tilde{\rho}_{yx}^{\text{int}} &= c\rho_{xx}^2,\end{aligned} \tag{2}$$

where $\Delta\tilde{\rho}_{yx}^{\text{skew}}$, $\Delta\tilde{\rho}_{yx}^{\text{sj}}$, $\Delta\tilde{\rho}_{yx}^{\text{int}}$ are contributions from the skew scattering, the side jump and the Berry curvature effect, respectively. a_1, a_2, b_1, b_2, b_3 and c are the scaling coefficients. In contrast to the note made in Ref. [39], here we have included a dynamic skew scattering (the a_2-term).

We first study the effect of static disorders on the anomalous Hall resistance. We set $\rho_{xx}^T = 0$ and rearrange Eq. (2) to obtain

$$\frac{\Delta\tilde{\rho}_{yx}^0}{\rho_{xx}^0} = a_1 + (b_1 + c)\rho_{xx}^0 \tag{3}$$

where $\Delta\tilde{\rho}_{yx}^0$ is $\Delta\tilde{\rho}_{yx}$ measured at the lowest temperature (2 K). In Fig. 4(d), we plot $\frac{\Delta\tilde{\rho}_{yx}^0}{\rho_{xx}^0}$ as a function of ρ_{xx}^0 to determine a_1 and $b_1 + c$. (As a reference, $\Delta\tilde{\rho}_{yx}^0$ vs. ρ_{xx}^0 is plotted in the inset.) Data is fitted with Eq. (3): the fitted curve is shown by the solid line. We find $a_1 \sim -0.034$ and $b_1 + c \sim 1.5 \times 10^{-4}$ (μΩ cm)$^{-1}$. These results show that films with larger ρ^0_{xx} exhibit positive $\Delta\tilde{\rho}^0_{yx}$ due to the larger contribution from the impurity induced side-jump/Berry curvature effect, i.e. the $b_1 + c$ term. This is the case for the thinner films. For the thicker films, $\Delta\tilde{\rho}^0_{yx}$ is negative since contribution from the impurity induced skew scattering (a_1 term) is larger.

Next, we look into the influence of dynamic disorders, which cause the temperature dependent anomalous Hall resistance. We find that most of the data ($\Delta\tilde{\rho}_{yx}$ vs. ρ_{xx}) can be described by a linear function, shown by the solid lines in Fig. 4(c), particularly when the film thickness is small. The predominant linear dependence indicates that skew scattering (the a_2 term in Eq. (2)) contributes to the anomalous Hall effect, consistent with previous reports on Cr-Te systems[14–16, 19]. We fit the data from 2 $\sim$ 100 K with a linear line. From Eq. (2), the slope of the linear line is equal to $a_2 + (b_3 + 2c)\rho^0_{xx}$. (Note that the slope of $\Delta\tilde{\rho}_{yx}$ vs. ρ^T_{xx} is the same as that of $\Delta\tilde{\rho}_{yx}$ vs. ρ_{xx} since ρ^0_{xx} is a constant.) We thus plot the slope as a function of ρ^0_{xx} in Fig. 4(e) and fit a linear function, which is shown by the solid line. From the fitting, we find $a_2 \sim -0.067$ and $b_3 + 2c \sim 0.7 \times 10^{-4}$ $(\mu\Omega$ cm$)^{-1}$. a_2 is comparable in magnitude with the skew scattering coefficient in other systems[41–43].

Before discussing the origin of the a_2 term, we comment on the other terms in the anomalous Hall resistivity. As is evident in Fig. 4(c), the data deviates from the linear fitting for the thicker films at higher temperatures. The deviation is caused by the side jump and/or Berry curvature contributions, i.e., b_2 and c terms in Eq. (2). (For the thinner films, because of the lower resistivity at high temperature, influence from the quadratic terms is limited.) A previous study showed that the Berry curvature contribution in Cr_2Te_3 can vary with temperature due to thermal broadening of the Fermi surface and may depend on the film thickness via growth induced strain[20, 23]: see Supplementary Note 3 and Figure S6 for the first principles calculations we performed as well. The possible change of the Berry curvature contribution with temperature and thickness make it difficult to extract the coefficients b_2 and c using Eq. (2). We therefore focus on the predominant linear term (a_2) and simply note that the combined contributions from the quadratic terms (b_2 and c) take a maximum of $\sim$ 25% for the thickest film near the Curie temperature, which is estimated from the deviation of $\Delta\tilde{\rho}_{yx}$ from the linear fitting.

To identify the source of the a_2 term, we plot $\Delta\tilde{\rho}^T_{yx} \equiv \Delta\tilde{\rho}_{yx} - \Delta\tilde{\rho}^0_{yx}$ as a function of

ρ_{xx}^m in Fig. 4(f). $\Delta\tilde{\rho}_{yx}^T$ is positively related to ρ_{xx}^m, particularly at higher temperatures, suggesting that magnons play a dominant role in the dynamic disorder induced scattering. To corroborate this observation, the H_z dependence of the Hall resistance is measured up to 140 kOe for the 65 nm-thick film. The results obtained at measurement temperatures of 5 K and 150 K are shown in Fig. 5(a,b). At low temperature [Fig. 5(a)], ρ_{yx} scales linearly with H_z for fields outside the hysteresis loop, whereas it varies in a non-linear fashion for higher temperature [Fig. 5(b)]. (ρ_{yx} that scales with H_z at large field is mostly caused by the ordinary Hall effect.) To display the effect more clearly, we fit the data with a linear function in the range of $H_z \sim 130 - 140$ kOe and subtracted it from the data. The subtracted data, defined as ρ'_{yx}, are shown in Fig. 5(c,d). ρ'_{yx} tends to decrease as $|H_z|$ increases when the temperature is high, whereas it is nearly constant in the entire field range for lower temperature. Previous studies have shown that large magnetic field suppresses excitation of magnons[33, 44]. The reduction of $\Delta\rho_{yx}$ at large H_z can therefore be attributed to decrease in magnon population. These results thus support the notion that electron-magnon scattering contributes to the anomalous Hall resistance at higher temperatures. We note that the saturation of ρ'_{yx} in Fig. 5(d) is caused by the linear background subtraction process. Measurements at even larger magnetic field are needed to determine the saturation field. Indeed, previous studies showed that suppression of magnon induced effects requires magnetic field of the order of a few hundreds of kOe[33]. Suppression of electron-magnon scattering by magnetic field can also be found in the magnetoresistance measured at higher magnetic field. Figure 5(e) shows the magnetoresistance $\Delta\rho_{xx}$ measured up to 140 kOe for the 65 nm-thick film. The slope of $\Delta\rho_{xx}$ vs. H_z clearly changes with H_z at higher temperatures. Note that the slope represents the strength of magnon scattering: see the discussion pertaining to Fig. 3. We plot the temperature dependence of the slope $\Delta\rho_{xx}/H_z$ at lower magnetic field (0-10 kOe) and higher magnetic field (130 -140 kOe) in Fig. 5(f). The former is significantly larger than the latter when the temperature is high, indicating that magnon excitation is suppressed at larger magnetic field. These results strongly suggest that the source of the a_2 term is magnon-induced skew scattering.

Based on these results, we discuss the reason behind the sign change of the anomalous Hall resistance with temperature in Cr_2Te_3. At the lowest temperature, $\Delta\tilde{\rho}_{yx}^0$ is governed by static disorder (impurity) ρ_{xx}^0. The linear (a_1) and quadratic ($b_1 + c$) terms have opposite sign. For the thinner films (with larger ρ_{xx}^0), the net contribution is positive since the quadratic term dominates. In contrast, $\Delta\tilde{\rho}^0_{yx}$ is negative for the thicker films (with smaller ρ^0_{xx}) as the linear term is dominant. With increasing temperature, contribution from the magnon induced skew scattering (a_2), which is negative, increases and takes over, resulting in a sign change of $\Delta\tilde{\rho}_{yx}$ only for the thinner films.

III. MODEL CALCULATIONS

Finally, we discuss the microscopic origin of the magnon induced skew scattering in Cr_2Te_3. The anomalous Hall resistivity $\Delta\tilde{\rho}_{yx}$ that originates from magnon induced skew scattering is obtained by including the effect of the spin-orbit coupling in a *p*-*d* exchange interaction. The Hamiltonian that describes the electron-magnon skew scattering has been proposed as[45]:

$$\mathcal{H}_{pd} = i\lambda J_{pd} a_0^2 \sum_{\boldsymbol{k},\boldsymbol{k}'} (\boldsymbol{k} \times \boldsymbol{k}') \cdot (\delta \boldsymbol{S})_{\boldsymbol{k}-\boldsymbol{k}'} \, c^\dagger_{\boldsymbol{k}} c_{\boldsymbol{k}'}, \tag{4}$$

where λ is a dimensionless parameter that characterizes the spin-orbit coupling, J_{pd} represents the *p*-*d* exchange interaction between the Te $5p$ conduction electrons and the Cr $3d$ localized moments, a_0^3 is the volume per localized spin, $\boldsymbol{k}$ and $c_{\boldsymbol{k}}$ are the electron wave vector and annihilation operator, $\boldsymbol{S}$ represents the localized spin ($|\boldsymbol{S}| = 3/2$ for Cr) and $\delta\boldsymbol{S}$ is the deviation from its equilibrium direction due to magnon excitation. Assuming a free electron like band with exchange splitting, the anomalous Hall resistivity $\Delta\tilde{\rho}^{\mathrm{cal}}_{yx}$ is calculated by considering the process shown in Supplementary Figure S7 , as

$$\Delta\tilde{\rho}^{\mathrm{cal}}_{yx} = -\Xi_{yx} \frac{\lambda a_0^2 J_{pd}^3 S}{8\hbar^2 e^2 v_{\mathrm{F}}^3} \left(\frac{k_{\mathrm{B}} T}{A_{\mathrm{ex}}}\right)^2 \tag{5}$$

where v_{F} is the Fermi velocity and A_{ex} is the exchange stiffness parameter. ($\hbar$ is the reduced Planck constant, e is the elementary charge and k_{B} is the Boltzmann constant.) Note that this process was not considered in Ref. [39]. The longitudinal resistivity ρ^{cal}_{xx} due to electron-magnon scattering is given by[45]

$$\rho^{\mathrm{cal}}_{xx} = \Xi_{xx} \frac{m^2 J_{pd}^2 S}{(2\pi)^3 \hbar^3 e^2 n^2 a_0^3} \left(\frac{k_{\mathrm{B}} T}{A_{\mathrm{ex}}}\right)^2 \tag{6}$$

where Ξ_{yx} [in Eq. (5)] and Ξ_{xx} [in Eq. (6)] are constants of order unity and weakly dependent on temperature (see Supplementary Figure S8). m is the effective electron mass and n is the electron density. See Supplementary Note 4 for the outline of the derivation of Eqs. (5)

and (6), details of Ξ_{yx} and Ξ_{xx} and the Feyman diagram (Supplementary Figure S7) used to calculate the anomalous Hall conductivity due to magnon scattering.

Both $\Delta\tilde{\rho}_{yx}^{\rm cal}$ and $\rho_{xx}^{\rm cal}$ scale with the temperature T quadratically, in agreement with the experiments: see Figs. 2(b) and 4(b). Substituting the parameters listed in Supplementary Table 1, suitable for Cr_2Te_3, we obtain $\Delta\tilde{\rho}_{yx}^{\rm cal} \sim -22$ $\mu\Omega$·cm and $\rho_{xx}^{\rm cal} \sim 329$ $\mu\Omega$·cm at $T = 200$ K from Eqs. (5) and (6). Here we adjusted λ, the dimensionless parameter that characterizes the spin-orbit interaction, to match the value of $a_2 = -0.067$ obtained in the experiments with $\Delta\tilde{\rho}_{yx}^{\rm cal}/(\rho_{xx}^{\rm cal})$. Note that $J_{pd} = -0.1$ eV is estimated from the band structure of Cr_2Te_3 using first principles calculations. J_{pd} is normally negative when the exchange coupling is between conduction electrons and localized moments that belong to different elements. From Eq. (5), we find λ must be negative in order to account for the negative $\Delta\tilde{\rho}_{yx}$ found in the experiments (see e.g. Fig. 4(b)). The strength of the $p-d$ exchange interaction, characterized by λJ_{pd}, is ~ 0.084 eV, which is similar in magnitude with the atomic spin-orbit coupling of Te[46–48]. We thus infer that the predominant magnon-induced skew scattering in Cr_2Te_3 is primarily induced by the large spin-orbit coupling of Te. A microscopic model that takes into account the band structure of host material (here Cr_2Te_3) is required to clarify the relation between the atomic spin orbit coupling and λ.

IV. CONCLUSION

We have studied the longitudinal and anomalous Hall resistivities of Cr_2Te_3 thin films. We find a quadratic temperature dependence of the longitudinal resistivity below the Curie temperature, suggesting that electron-magnon scattering is one of the major sources of the resistivity. This is corroborated by a linear magnetoresistance found against the out-of-plane magnetic field. The anomalous Hall resistivity includes two major contributions: temperature dependent and temperature independent terms. The former exhibits a predominant linear dependence with the longitudinal resistivity and is positively correlated with the electron-magnon scattering coefficient of the longitudinal resistivity, suggesting that magnon induced skew scattering significantly contributes to the anomalous Hall effect in Cr_2Te_3. We also find the anomalous Hall resistivity at higher temperature is suppressed by large magnetic field, supporting the scenario that the skew scattering originates from collision with magnons. For the latter (i.e. the temperature independent term), we find that the contribution from the impurity induced side-jump and/or the Berry curvature effect possess the opposite sign with that of magnon-induced skew scattering. The sign change of the anomalous Hall resistivity with temperature is thus accounted for by the competition between the two effects. Using model calculations, we show that the *p*-*d* type exchange interaction modified by spin-orbit coupling can account for the significant electron-magnon scattering contribution to the anomalous Hall effect in Cr_2Te_3. These results suggest that magnon-induced skew scattering plays a significant role in the anomalous Hall effect in layered ferromagnets with heavy elements, a class of 2D materials that are of current interest.

ACKNOWLEDGMENTS

This work was partly supported by JSPS KAKENHI (Grant Numbers 21H01608, 22K14290, 22K18935, 23H00176, 23H05463), JST CREST (JPMJCR19T3), MEXT Initiative to Establish Next-generation Novel Integrated Circuits Centers (X-NICS) and Cooperative Research Project Program of RIEC, Tohoku University. Computations were performed on a Numerical Materials Simulator at NIMS. Y.W. is supported by the GSGC program of University of Tokyo, S.W. thanks JST SPRING GX, Grant Number JPMJSP2108.

Author contributions

Y.W. deposited the films, fabricated the samples and performed the magnetic and transport measurements, with the help of M.K. S.W. helped the film growth and the RHEED observation. A.K.P. and Y.S. carried out the high field transport measurements. J.U. and T.O. fabricated the specimen and conducted the HAADF-STEM observation. K.N. performed the first principles calculations and H.K. carried out the model calculations. Y.W. and M.H. wrote the manuscript with substantial inputs from all authors.

Competing interests

The authors declare no competing interests.

Additional information

Supplementary information: The online version contains supplementary material available at XX.

V. METHODS

A. Sample preparation

Cr_2Te_3 films were grown on sapphire (0001) or MgO (001) substrates in a commercial molecular beam epitaxy (MBE) system. The substrates were pre-annealed in vacuum at 650 °C for 150 min for degassing. After degassing, the substrate temperature T_s was set to $\sim$ 380 °C. Tellurium and chromium were co-evaporated using a Knudsen cell for Te and an electron beam gun for Cr. To form Cr_2Te_3, the flux ratio of Te over Cr was kept to $\sim$20 or higher. The growth rate of Cr_2Te_3 was monitored using a quartz crystal spectrometer and its typical value is $\sim$0.01 nm/s. Cr_2Te_3 thin films with different thicknesses (5, 10, 26, 49 and 65 nm) were grown. The thickness of the films were determined using X-ray reflectivity measurements. A 5 nm-thick Te or 3 nm-thick Ti capping layer was deposited at room temperature to protect the Cr_2Te_3 film from oxidation. We find the type of substrate (sapphire vs. MgO) and the capping layer material (Te vs. Ti) have little influence on the magnetic and transport properties of the films.

B. Sample characterization

Magnetic properties of the films were examined by superconducting quantum interference diffractometer (SQUID). The specimen for cross-sectional transmission electron microscopy (TEM) studies was prepared by using a focused ion beam (FIB). High-angle annular dark-field scanning transmission electron microscopy (HAADF-STEM) observation, nanobeam electron diffraction, and energy dispersive x-ray spectroscopy (EDS) analysis were carried out using a commercial system.

To study the transport properties, the films were patterned into Hall bars using optical lithography and Ar ion milling. Contact electrodes, made of $\sim$50 nm thick conducting materials, were patterned on the Hall bars using standard liftoff technique. The electrodes were deposited via RF magnetron sputtering. The width w and length L of the Hall bar channel are 10 μm and 25 μm, respectively. Measurements were performed using a physical property measurement system (PPMS). A current I_x of 100 μA was applied to the sample and the longitudinal voltage V_{xx} and the transverse voltage V_{yx} were measured. The longitudinal and transverse resistivities are obtained from the relations $\rho_{xx} = \frac{V_{xx}}{I_x}\frac{wt}{L}$ and $\rho_{yx} = \frac{V_{yx}t}{I_x}$, respectively, where t is the thickness of the film. See Supplementary Note 2 and Figure S3 for the details of the configuration used to measure the longitudinal and transverse resistivities.

Data availability

Experimental data presented in the main text are stored in the Supplementary Data. All relevant data are available from the authors upon request.

References

[1] H. Ipser, K. L. Komarek, and K. O. Klepp, "Transition metal-chalcogen systems viii: The cr-te phase diagram," Journal of the Less Common Metals **92**, 265 (1983).

[2] M. A. McGuire, V. O. Garlea, K. C. Santosh, V. R. Cooper, J. Q. Yan, H. B. Cao, and B. C. Sales, "Antiferromagnetism in the van der waals layered spin-lozenge semiconductor $crte_3$," Phys. Rev. B **95**, 144421 (2017).

[3] Y. Fujisawa, M. Pardo-Almanza, J. Garland, K. Yamagami, X. Zhu, X. Chen, K. Araki, T. Takeda, M. Kobayashi, Y. Takeda, C. H. Hsu, F. C. Chuang, R. Laskowski, K. H. Khoo, A. Soumyanarayanan, and Y. Okada, "Tailoring magnetism in self-intercalated $cr_{1+\delta}te_2$ epitaxial films," Phys. Rev. Mater. **4**, 114001 (2020).

[4] X. Q. Zhang, Q. S. Lu, W. Q. Liu, W. Niu, J. B. Sun, J. Cook, M. Vaninger, P. F. Miceli, D. J. Singh, S. W. Lian, T. R. Chang, X. Q. He, J. Du, L. He, R. Zhang, G. Bian, and Y. B. Xu, "Room-temperature intrinsic ferromagnetism in epitaxial $crte_2$ ultrathin films," Nat. Commun. **12**, 2492 (2021).

[5] Bevin Huang, Genevieve Clark, Efren Navarro-Moratalla, Dahlia R. Klein, Ran Cheng, Kyle L. Seyler, Ding Zhong, Emma Schmidgall, Michael A. McGuire, David H. Cobden, Wang Yao, Di Xiao, Pablo Jarillo-Herrero, and Xiaodong Xu, "Layer-dependent ferromagnetism in a van der waals crystal down to the monolayer limit," Nature **546**, 270–273 (2017).

[6] Cheng Gong, Lin Li, Zhenglu Li, Huiwen Ji, Alex Stern, Yang Xia, Ting Cao, Wei Bao, Chenzhe Wang, Yuan Wang, Z. Q. Qiu, R. J. Cava, Steven G. Louie, Jing Xia, and Xiang Zhang, "Discovery of intrinsic ferromagnetism in two-dimensional van der waals crystals," Nature **546**, 265–269 (2017).

[7] M. Gibertini, M. Koperski, A. F. Morpurgo, and K. S. Novoselov, "Magnetic 2d materials and heterostructures," Nat. Nanotechnol. **14**, 408–419 (2019).

[8] J. C. Zhong, M. S. Wang, T. Liu, Y. H. Zhao, X. Xu, S. S. Zhou, J. B. Han, L. Gan, and T. Y. Zhai, "Strain-sensitive ferromagnetic two-dimensional cr_2te_3," Nano Research **15**, 1254 (2022).

[9] H. X. Li, L. J. Wang, J. S. Chen, T. Yu, L. Zhou, Y. Qiu, H. T. He, F. Ye, T. K. Sou, and G. Wang, "Molecular beam epitaxy grown cr_2te_3 thin films with tunable curie temperatures

for spintronic devices," Acs Applied Nano Materials **2**, 6809 (2019).

[10] Y. Wen, Z. H. Liu, Y. Zhang, C. X. Xia, B. X. Zhai, X. H. Zhang, G. H. Zhai, C. Shen, P. He, R. Q. Cheng, L. Yin, Y. Y. Yao, M. G. Sendeku, Z. X. Wang, X. B. Ye, C. S. Liu, C. Jiang, C. X. Shan, Y. W. Long, and J. He, "Tunable room-temperature ferromagnetism in two-dimensional cr_2te_3," Nano Lett. **20**, 3130–3139 (2020).

[11] R. Chua, J. Zhou, X. J. Yu, W. Yu, J. Gou, R. Zhu, L. Zhang, M. Z. Liu, M. B. H. Breese, W. Chen, K. P. Loh, Y. P. Feng, M. Yang, Y. L. Huang, and A. T. S. Wee, "Room temperature ferromagnetism of monolayer chromium telluride with perpendicular magnetic anisotropy," Adv. Mater. **33**, 2103360 (2021).

[12] A. L. Coughlin, D. Y. Xie, Y. Yao, X. Zhan, Q. Chen, H. Hewa-Walpitage, X. H. Zhang, H. Guo, H. D. Zhou, J. Lou, J. Wang, Y. S. Li, H. A. Fertig, and S. X. Zhang, "Near degeneracy of magnetic phases in two-dimensional chromium telluride with enhanced perpendicular magnetic anisotropy," ACS Nano **14**, 15256 (2020).

[13] M. Y. Bian, A. N. Kamenskii, M. J. Han, W. J. Li, S. C. Wei, X. Z. Tian, D. B. Eason, F. Sun, K. K. He, H. L. Hui, F. Yao, R. Sabirianov, J. P. Bird, C. L. Yang, J. W. Miao, J. H. Lin, S. A. Crooker, Y. L. Hou, and H. Zeng, "Covalent 2d cr2te3 ferromagnet," Mater. Res. Lett. **9**, 205–212 (2021).

[14] Y. Liu and C. Petrovic, "Anomalous hall effect in the trigonal cr_5te_8 single crystal," Phys. Rev. B **98**, 195122 (2018).

[15] Z. Z. Jiang, X. Luo, J. Yan, J. J. Gao, W. Wang, G. C. Zhao, Y. Sun, J. G. Si, W. J. Lu, P. Tong, X. B. Zhu, W. H. Song, and Y. P. Sun, "Magnetic anisotropy and anomalous hall effect in monoclinic single crystal cr_5te_8," Phys. Rev. B **102**, 144433 (2020).

[16] M. Huang, S. S. Wang, Z. H. Wang, P. Liu, J. X. Xiang, C. Feng, X. Q. Wang, Z. M. Zhang, Z. C. Wen, H. J. Xu, G. Q. Yu, Y. L. Lu, W. S. Zhao, S. Y. A. Yang, D. Z. Hou, and B. Xiang, "Colossal anomalous hall effect in ferromagnetic van der waals $crte_2$," Acs Nano **15**, 9759–9763 (2021).

[17] Y. Z. Sun, P. F. Yan, J. A. Ning, X. Q. Zhang, Y. F. Zhao, Q. W. Gao, M. Kanagaraj, K. P. Zhang, J. J. Li, X. Y. Lu, Y. Yan, Y. Li, Y. B. Xu, and L. He, "Ferromagnetism in two-dimensional $crte_2$ epitaxial films down to a few atomic layers," Aip Advances **11**, 035138 (2021).

[18] Y. X. Ou, W. Yanez, R. Xiao, M. Stanley, S. Ghosh, B. Y. Zheng, W. Jiang, Y. S. Huang,

T. Pillsbury, A. Richardella, C. X. Liu, T. Low, V. H. Crespi, K. A. Mkhoyan, and N. Samarth, "Zrte$_2$/crte$_2$: an epitaxial van der waals platform for spintronics," Nat. Commun. **13**, 2972 (2022).

[19] S. W. Cho, I. H. Lee, Y. W. Lee, S. Kim, Y. G. Khim, S. Y. Park, Y. Jo, J. Choi, S. W. Han, Y. J. Chang, and S. Y. Lee, "Investigation of the mechanism of the anomalous hall effects in cr$_2$te$_3$/(bisb)$_2$(tese)$_3$ heterostructure," Nano Convergence **10**, 2 (2023).

[20] H. Chi, Y. B. Ou, T. B. Eldred, W. P. Gao, S. Kwon, J. Murray, M. Dreyer, R. E. Butera, A. C. Foucher, H. Ambaye, J. Keum, A. T. Greenberg, Y. H. Liu, M. R. Neupane, G. J. de Coster, O. A. Vail, P. J. Taylor, P. A. Folkes, C. R. Rong, G. Yin, R. K. Lake, F. M. Ross, V. Lauter, D. Heiman, and J. S. Moodera, "Strain-tunable berry curvature in quasi-two-dimensional chromium telluride," Nat. Commun. **14**, 3222 (2023).

[21] K. K. He, M. Y. Bian, S. D. Seddon, K. Jagadish, A. Mucchietto, H. Ren, E. Kirstein, R. Asadi, J. Bai, C. Yao, S. Pan, J. X. Yu, P. Milde, C. Huai, H. L. Hui, J. D. Zang, R. Sabirianov, X. M. M. Cheng, G. X. Miao, H. Xing, Y. T. Shao, S. A. Crooker, L. Eng, Y. L. Hou, J. P. Bird, and H. Zeng, "Unconventional anomalous hall effect driven by self-intercalation in covalent 2d magnet cr$_2$te$_3$," Adv. Sci. (2024).

[22] Y. Fujisawa, M. Pardo-Almanza, C. H. Hsu, A. Mohamed, K. Yamagami, A. Krishnadas, G. Q. Chang, F. C. Chuang, K. H. Khoo, J. D. Zang, A. Soumyanarayanan, and Y. Okada, "Widely tunable berry curvature in the magnetic semimetal cr$_{1+\delta}$te$_2$," Adv. Mater. **35** (2023).

[23] A. K. Song, J. E. Zhang, Y. Q. Chen, Z. Z. Zhang, X. J. Cheng, R. J. Xu, W. Z. Zhuang, W. X. Sun, Y. Zhang, X. Zhang, Z. Q. Chen, F. Q. Song, Y. Zhang, X. C. Zhai, Y. B. Xu, W. S. Zhao, R. Zhang, and X. F. Wang, "Large anomalous hall effect in a noncoplanar magnetic heterostructure," Adv. Funct. Mater. (2025).

[24] M. Huang, Z. W. Ma, S. Wang, S. Li, M. Li, J. X. Xiang, P. Liu, G. J. Hu, Z. M. Zhang, Z. Sun, Y. L. Lu, Z. G. Sheng, G. Chen, Y. L. Chueh, S. Y. Yang, and B. Xiang, "Significant perpendicular magnetic anisotropy in room-temperature layered ferromagnet of cr-intercalated crte$_2$," 2d Materials **8**, 031003 (2021).

[25] K. Lasek, P. M. Coelho, K. Zberecki, Y. Xin, S. K. Kolekar, J. F. Li, and M. Batzill, "Molecular beam epitaxy of transition metal (ti-, v-, and cr-) tellurides: From monolayer ditellurides to multilayer self-intercalation compounds," Acs Nano **14**, 8473–8484 (2020).

[26] J. Dijkstra, H. H. Weitering, C. F. Vanbruggen, C. Haas, and R. A. Degroot, "Band-structure

calculations, and magnetic and transport properties of ferromagnetic chromium tellurides (crte, cr3te4, cr2te3)," J. Phys.: Cond. Matt. **1**, 9141–9161 (1989).

[27] C. H. Zhang, C. Liu, J. W. Zhang, Y. Y. Yuan, Y. Wen, Y. Li, D. X. Zheng, Q. Zhang, Z. P. Hou, G. Yin, K. Liu, Y. Peng, and X. X. Zhang, "Room-temperature magnetic skyrmions and large topological hall effect in chromium telluride engineered by self-intercalation," Adv. Mater. **35** (2023).

[28] Y. Wang, S. Kajihara, H. Matsuoka, B. K. Saika, K. Yamagami, Y. Takeda, H. Wadati, K. Ishizaka, Y. Iwasa, and M. Nakano, "Layer-number-independent two-dimensional ferromagnetism in cr3te4," Nano Lett. **22**, 9964–9971 (2022).

[29] J. F. Yang, J. W. Ng, C. Zhu, Y. Wu, J. Y. Shi, R. J. Sun, and B. J. Tang, "Chemical vapor deposition of large-area ultrathin cr3te4 nanosheets with robust ferromagnetism," 2d Materials **12**, 015002 (2025).

[30] L. D. Tung, V. Kolesnichenko, D. Caruntu, N. H. Chou, C. J. O'Connor, and L. Spinu, "Magnetic properties of ultrafine cobalt ferrite particles," J. Appl. Phys. **93**, 7486–7488 (2003).

[31] I. Mannari, "Electrical resistance of ferromagnetic metals," Prog. Theor. Phys. **22**, 335 (1959).

[32] Volkenshtein Nv, V. P. Dyakina, and V. E. Startsev, "Scattering mechanisms of conduction electrons in transition metals at low temperatures," Phys. Status Solidi B **57**, 9– (1973).

[33] B. Raquet, M. Viret, E. Sondergard, O. Cespedes, and R. Mamy, "Electron-magnon scattering and magnetic resistivity in $3d$ ferromagnets," Phys. Rev. B **66**, 024433 (2002).

[34] Y. Q. Chen, Y. M. Zhu, R. J. Lin, W. Niu, R. X. Liu, W. Z. Zhuang, X. Zhang, J. H. Liang, W. X. Sun, Z. Q. Chen, Y. S. Hu, F. Q. Song, J. Zhou, D. Wu, B. H. Ge, H. X. Yang, R. Zhang, and X. F. Wang, "Observation of colossal topological hall effect in noncoplanar ferromagnet cr5te6 thin films," Adv. Funct. Mater. **33** (2023).

[35] X. Q. Zhang, S. C. Ambhire, Q. S. Lu, W. Niu, J. Cook, J. S. Jiang, D. S. Hong, L. Alahmed, L. He, R. Zhang, Y. B. Xu, S. S. L. Zhang, P. Li, and G. Bian, "Giant topological hall effect in van der waals heterostructures of crte2/bi2te3," Acs Nano **15**, 15710–15719 (2021).

[36] J. H. Jeon, H. R. Na, H. Kim, S. Lee, S. Song, J. Kim, S. Park, J. Kim, H. Noh, G. Kim, S. K. Jerng, and S. H. Chun, "Emergent topological hall effect from exchange coupling in ferromagnetic cr2te3/ noncoplanar antiferromagnetic cr2se3 bilayers," Acs Nano **16**, 8974–8982 (2022).

[37] N. Nagaosa, J. Sinova, S. Onoda, A. H. MacDonald, and N. P. Ong, "Anomalous hall effect,"

Rev. Mod. Phys. **82**, 1539–1592 (2010).

[38] Y. Tian, L. Ye, and X. F. Jin, "Proper scaling of the anomalous hall effect," Phys. Rev. Lett. **103**, 087206 (2009).

[39] D. Z. Hou, G. Su, Y. Tian, X. F. Jin, S. Y. A. Yang, and Q. Niu, "Multivariable scaling for the anomalous hall effect," Phys. Rev. Lett. **114**, 217203 (2015).

[40] V. L. Grigoryan, J. Xiao, X. H. Wang, and K. Xia, "Anomalous hall effect scaling in ferromagnetic thin films," Phys. Rev. B **96**, 144426 (2017).

[41] E. V. Vidal, H. Schneider, and G. Jakob, "Influence of disorder on anomalous hall effect for heusler compounds," Phys. Rev. B **83**, 174410 (2011).

[42] M. S. Gabor, M. Belmeguenai, T. Petrisor, C. Ulhaq-Bouillet, S. Colis, and C. Tiusan, "Correlations between structural, electronic transport, and magnetic properties of $co_2feal_0.5si_0.5$ heusler alloy epitaxial thin films," Phys. Rev. B **92**, 054433 (2015).

[43] K. K. Meng, J. Miao, X. G. Xu, J. H. Zhao, and Y. Jiang, "Thickness dependence of magnetic anisotropy and intrinsic anomalous hall effect in epitaxial co_2mnal film," Phys. Lett. A **381**, 1202–1206 (2017).

[44] T. Kikkawa, K. Uchida, S. Daimon, Z. Y. Qiu, Y. Shiomi, and E. Saitoh, "Critical suppression of spin seebeck effect by magnetic fields," Phys. Rev. B **92**, 064413 (2015).

[45] V. Yu. Irkhin and Yu. P. Irkhin, "Electronic structure, correlation effects and physical properties of d- and f-metals and their compounds," (2021), arXiv:cond-mat/9812072 [cond-mat].

[46] T. Doi, K. Nakao, and H. Kamimura, "Valence band structure of tellurium .1. k.p perturbation method," J. Phys. Soc. Jpn. **28**, 36 (1970).

[47] T. Furukawa, Y. Shimokawa, K. Kobayashi, and T. Itou, "Observation of current-induced bulk magnetization in elemental tellurium," Nat. Commun. **8**, 954 (2017).

[48] M. Sakano, M. Hirayama, T. Takahashi, S. Akebi, M. Nakayama, K. Kuroda, K. Taguchi, T. Yoshikawa, K. Miyamoto, T. Okuda, K. Ono, H. Kumigashira, T. Ideue, Y. Iwasa, N. Mitsuishi, K. Ishizaka, S. Shin, T. Miyake, S. Murakami, T. Sasagawa, and T. Kondo, "Radial spin texture in elemental tellurium with chiral crystal structure," Phys. Rev. Lett. **124**, 136404 (2020).

Figure captions

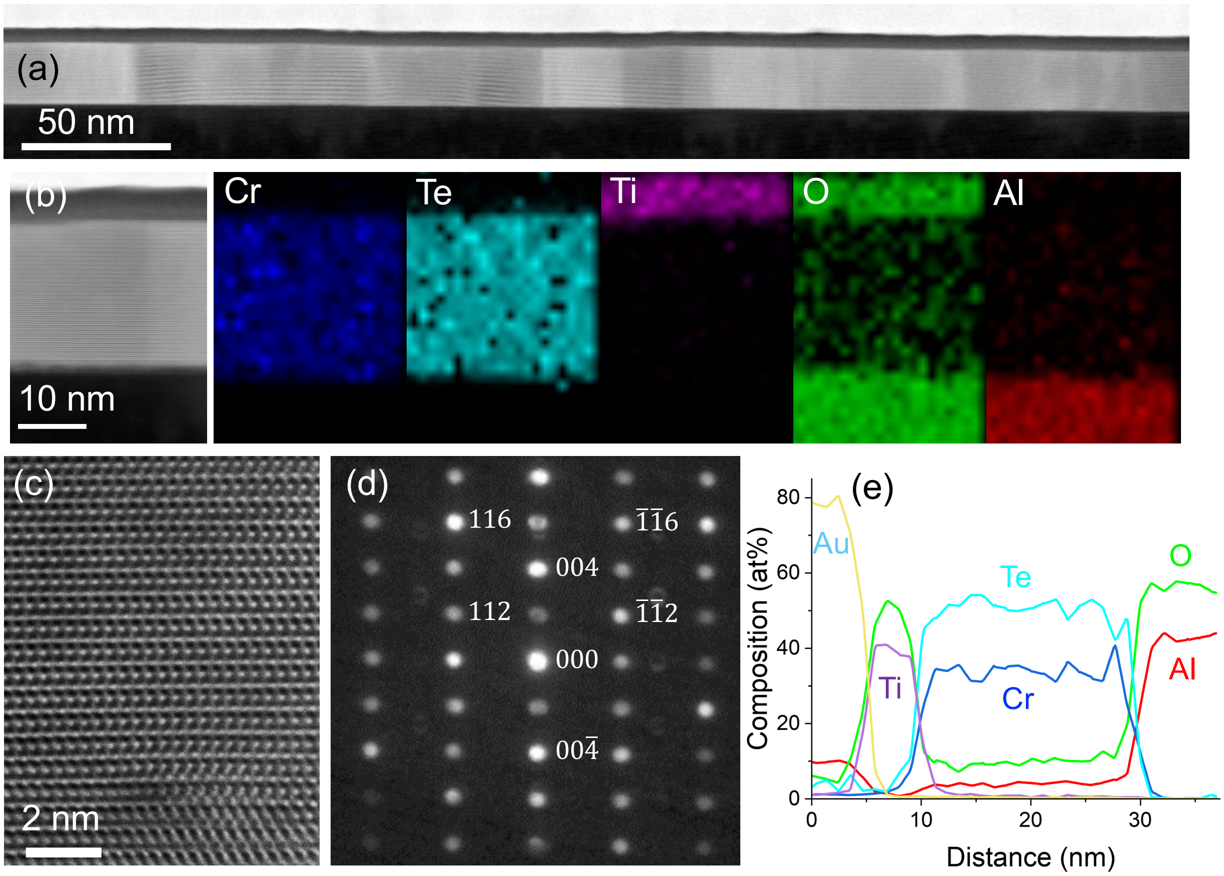

FIG. 1. **Structural characterization.** (a) Cross-sectional high-angle annular dark-field scanning transmission electron microscopy (HAADF-STEM) image and (b) EDS maps of a 20 nm-thick Cr_2Te_3 film. (c) High magnification image of the Cr_2Te_3 film shown in (a). (d) Nanobeam electron diffraction pattern of the image shown in (c). Indices of Cr_2Te_3 are labeled. (e) Depth profile of the elements using energy dispersive X-ray spectroscopy (EDS) mapping.

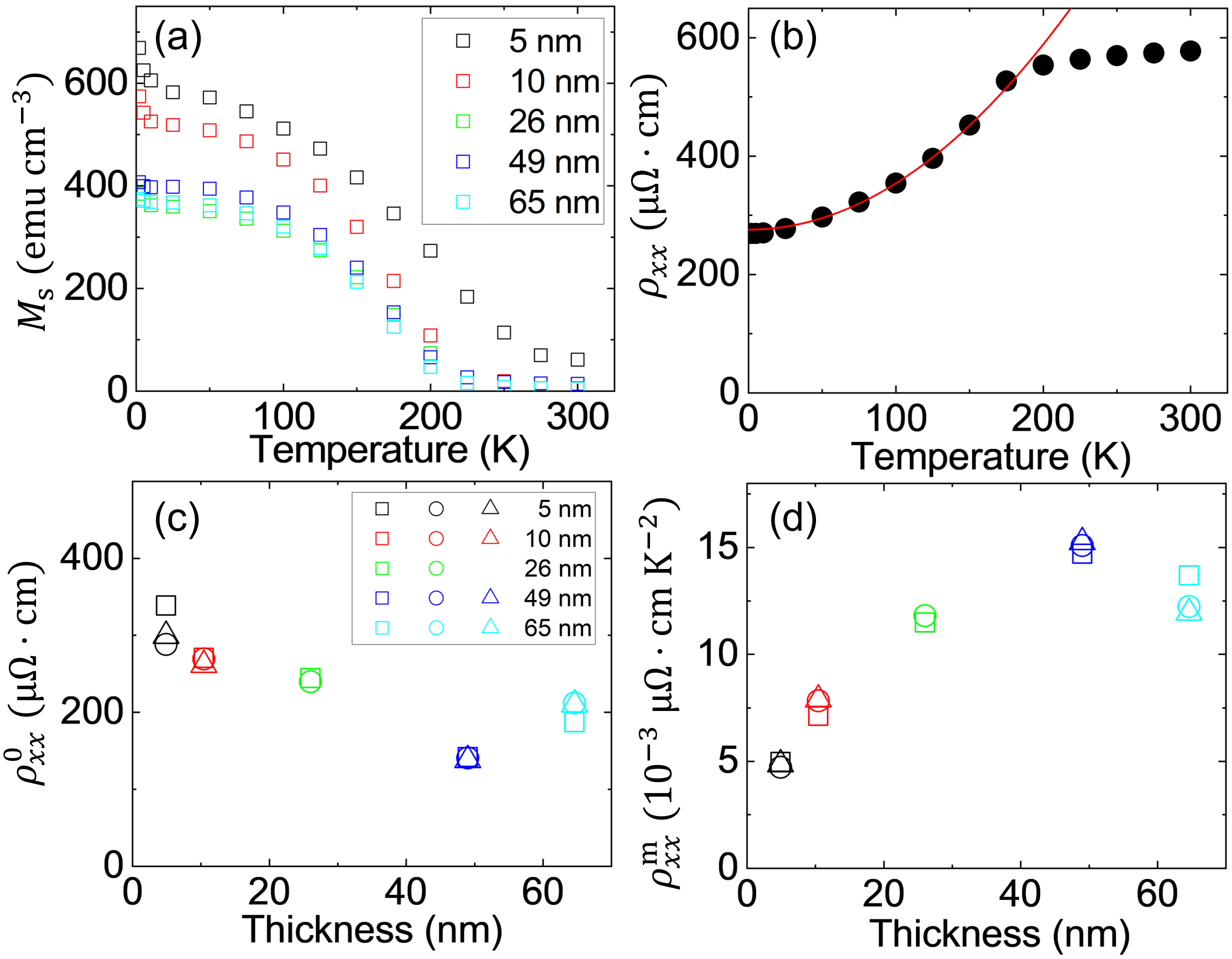

FIG. 2. **Saturation magnetization and longitudinal resistivity.** (a) Temperature T dependence of the saturation magnetization M_s for films with different thicknesses. (b) Longitudinal resistivity ρ_{xx} of a 10 nm-thick Cr_2Te_3 film plotted against T. The solid red line shows fit to the data using Eq. (1) in the appropriate temperature range. (c,d) Film thickness dependence of the impurity scattering coefficient ρ^0_{xx} (c) and the electron-magnon scattering coefficient ρ^m_{xx} (d). For a given film thickness, results from a few devices are presented using different symbols. Definition of the symbols are the same for panels (c,d): see the legend shown in (c).

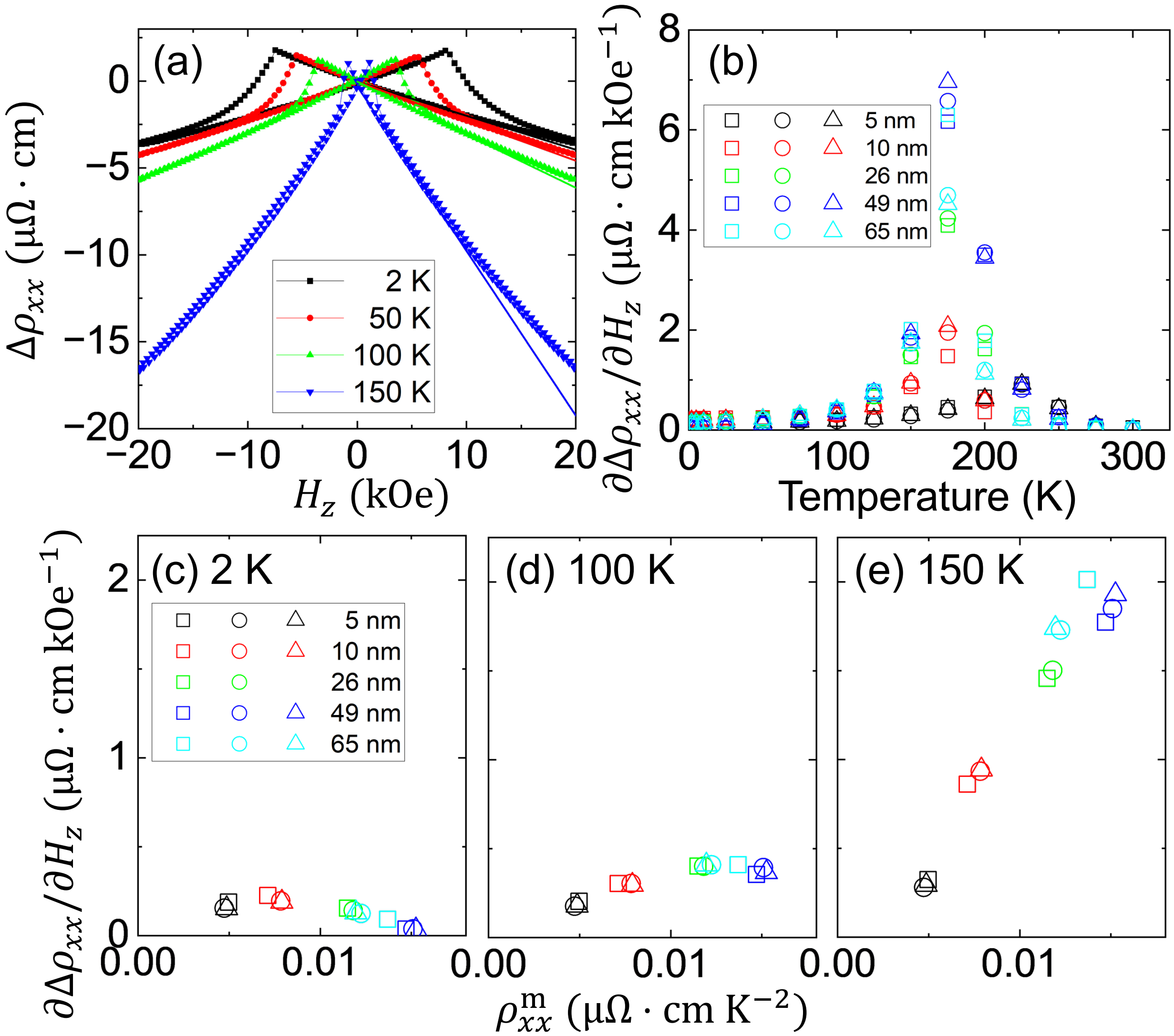

FIG. 3. **Longitudinal magnetoresistance.** (a) Magnetoresistance $\Delta\rho_{xx}$ as a function of out of plane magnetic field H_z obtained for a 10 nm-thick film. Different symbols indicate different measurement temperatures. The solid lines show linear fits to the data when H_z is in the range of 0 to 10 kOe. (b) Slope of fitted linear line, $\frac{\partial\Delta\rho_{xx}}{\partial H_z}$, plotted as a function of temperature. (c-e) Electron-magnon scattering coefficient ρ_{xx}^{m} dependence of $\frac{\partial\Delta\rho_{xx}}{\partial H_z}$ obtained at 2 K (c), 100 K (d) and 150 K (e). (b-e) For a given film thickness, results from a few devices are presented using different symbols. Definition of the symbols are the same for panels (c-e): see the legend shown in (c).

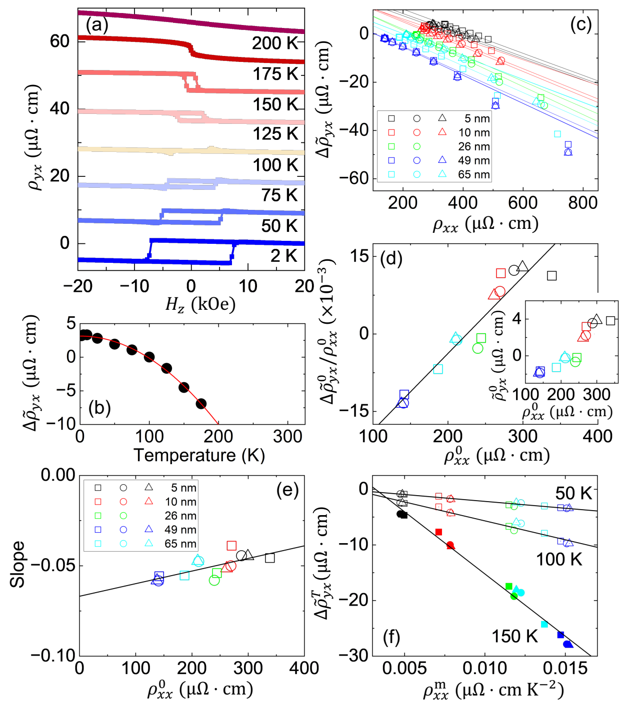

FIG. 4. **Anomalous Hall resistivity.** (a) Transverse resistivity ρ_{yx}, measured at different temperatures, is plotted against the out of plane magnetic field H_z for a 10 nm-thick Cr_2Te_3 film. Data are shifted vertically for clarity. (b) Normalized anomalous Hall resistivity $\Delta\tilde{\rho}_{yx} = \Delta\rho_{yx}/\frac{M_s}{M_s^0}$ (black circles) of a 10 nm-thick Cr_2Te_3 film plotted against the temperature T. Red solid lines show a parabolic fitting to the data. (c) The symbols indicate the longitudinal resistivity ρ_{xx} dependence of $\Delta\tilde{\rho}_{yx}$. Data displayed are from a temperature range of 2 K to 175 K. Fit to the data with a linear function is shown by the solid lines. (d) $\frac{\Delta\tilde{\rho}^0_{yx}}{\rho^0_{xx}}$ plotted against the impurity scattering coefficient ρ^0_{xx} (symbols). The solid line shows fit to the data using Eq. (3). The inset shows $\Delta\tilde{\rho}^0_{yx}$, i.e. $\Delta\tilde{\rho}_{yx}$ obtained at the lowest temperature, plotted as a function of ρ^0_{xx}. Definition of the symbols are the same as in (c): see the legend shown in (c). (e) The slope of the linear function used to fit the data shown in (c) plotted against ρ^0_{xx} (symbols). The solid line is a linear fit to the data. (f) $\Delta\tilde{\rho}^T_{yx} \equiv \Delta\tilde{\rho}_{yx} - \Delta\tilde{\rho}^0_{yx}$ plotted as a function of electron-magnon scattering coefficient ρ^{m}_{xx}. The open, dot center and solid symbols show data obtained at temperatures of $50, 100, 150$ K, respectively. The color of the symbols represents the film thickness whereas the symbol shape indicates results from different devices: see the legend shown in (e). The solid linear lines are guide to the eye. (c-f) For a given film thickness, results from a few devices are presented using different symbols.

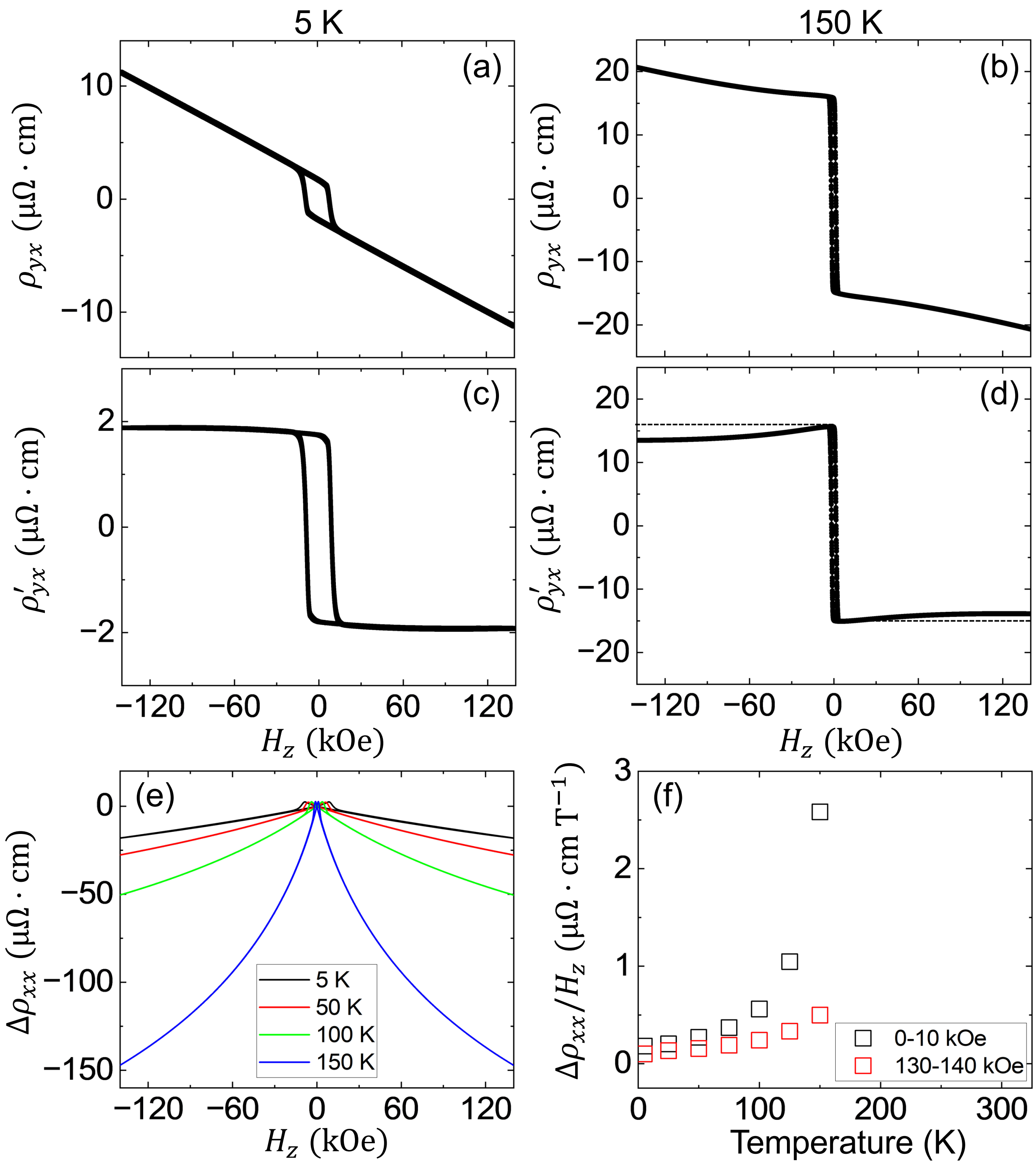

FIG. 5. **High field longitudinal and transverse resistivities.** (a,b) Transverse resistivity ρ_{yx} vs. out of plane magnetic field H_z measured at 2 K (a) and 150 K (b) for a 65 nm-thick film. (c,d) H_z dependence of the linear background subtracted transverse resistivity ρ'_{yx}. The background is determined by fitting the data in the field range of 130-140 kOe with a linear function. The horizontal dotted line in (d) is a guide to the eye. (e) H_z dependence of the magnetoresistance $\Delta\rho_{xx}$ of a 65 nm sample measured up to 140 kOe. (f) The slope of the linear line fitted to $\Delta\rho_{xx}$ vs. H_z in field ranges 0-10 kOe (black squares) and 130-140 kOe (red circles) are plotted as a function of temperature.